Volume 19, Number 1, 2026. pp. 55-63

Jordan Journal of Physics

ARTICLE

# Optical Analysis of Co-doped ZnO Thin Films Based on Nanoparticles

**N. Khlifi**[a], **O. Toulemonde**[b], **N. Ihzaz**[a], **M. N. Bessadok**[a], **M. Nouiri**[a] and **L. El Mir**[a]

[a] *Laboratory of Physics of Materials and Nanomaterials Applied at Environment (LaPhyMNE), Gabes University, 6072 Faculty of Sciences in Gabes, Tunisia.*

[b] *ICMCB-CNRS – Université de Bordeaux 87, Avenue du Dr. Albert Schweitzer, 33608, Pessac Cedex, France.*

***DOI:*** **https://doi.org/10.47011/19.1.6**

*Received on: 05/11/2024; Accepted on: 12/06/2025*

**Abstract:** The effect of cobalt doping with a concentration of 3 at. % on the structural and optical properties of ZnO oxide nanoparticles (NPs) prepared via a modified sol-gel method was investigated. X-ray diffraction analysis using Rietveld refinement confirms the hexagonal wurtzite ZnO phase nanostructure belonging to P63mc space group. No segregated secondary phases or Co-rich clusters were detected. In the second step, the obtained powders were deposited on a Suprasil glass substrate by the pulsed laser deposition technique. X-ray diffraction with Rietveld refinement confirms that the thin film exhibits an intense (002) XRD peak, indicating that it has a c-axis-preferred orientation. Raman studies confirm the crystalline nature of Co-doped ZnO thin films and nanoparticles. The combination of these two synthesis techniques demonstrates the potential of the protocol for the deposition of thin layers with adjusted properties.

**Keywords:** Nanoparticles, Thin film, Pulsed laser deposition technique, Gap energy, Raman spectra.

## 1. Introduction

The relationship between the physical and microstructural properties of solids has been studied for many years, and it is undeniable that nanostructured materials exhibit a wide range of properties with distinct applications that are influenced by their microstructural characteristics [1-4]. With different metal oxides considered as potential possibilities, zinc oxide (ZnO) nanoparticles have a wide range of applications. Zinc oxide is an II-VI n-type semiconductor, has a broadband gap energy of 3.37 eV, is transparent in the visible and near-infrared, and has an exciton binding energy of 60 meV. It also has a high piezoelectric effect and substantial electron mobility. Zinc oxide has been widely applied in the field of prospective optoelectronic applications such as gas sensors, nanogenerators, photodiodes, varistors, and light-emitting diodes [5-8]. ZnO powder has been synthesized using various techniques to create thin films by spray pyrolysis, electron beam evaporation, pulsed laser deposition (PLD), sol-gel, chemical vapor deposition (CVD), RF magnetron sputtering, and the hydrothermal process [9-13]. Doping with magnetic ions can induce room-temperature ferromagnetism [14-17]. The role of doping with metals is a preferred approach for tuning to control, for example, the band gap for oxide semiconductors [18]. In addition, doping with transition metals is an effective way to improve and adjust structural, optical, and magnetic properties [19]. This study focused on Co-doped ZnO, which is an n-type diluted magnetic semiconductor (DMS). It is part of a widely explored field, but it presents several innovative

**Corresponding Author:** Najet Khlifi **Email**: Khlifinajet45@gmail.com
Lassaad EL MIR **Email**: Lassaad.ElMir@fsg.rnu.tn

facets that make it different from previous works. Rather than focusing on a single fabrication method, we have adopted a two-step approach combining sol-gel synthesis of nanoparticles and pulsed laser deposition to elaborate thin films. This approach improves the material's structural and optical properties. In addition, our work features a detailed comparison between nanoparticles and Co-doped ZnO thin films, highlighting the variations induced by the deposition technique on crystallographic, optical, and morphological characteristics. This comparative analysis is essential for the development of specific optoelectronic applications. In addition, we have carried out detailed characterization of our samples using X-ray diffraction with Rietveld refinement, Raman spectroscopy and the study of optical properties via UV-Visible spectroscopy, offering a finer understanding of the effects of doping and the deposition process.

## 2. Materials and Processing

We first prepared $Zn_{1-x}Co_xO$ (x = 0.03) nanoparticles by sol-gel method according to the El Mir et al. process [20, 21]: 16 g of zinc acetate dihydrate [$Zn(CH_3COO)_2 \cdot 2H_2O$] was dissolved in 112 mL of methanol. After 10 min of magnetic stirring at room temperature, an amount of cobalt acetate [$(CH_3COO_2)\ CO.4H_2O$] was added. After 15 min of magnetic stirring, this solution was placed in an autoclave. It was then dried in supercritical conditions after adding 188 mL of ethyl alcohol (EtOH) ($T_c$ = 250 °C, $P_c$ = 80 bar). For the preparation of thin film, the Co-doped zinc oxide 3 at. % nanopowder was deposited on a Suprasil substrate by pulsed laser deposition technique (PLD/MBE 2100) from PVD products [22], and the source was a KrF excimer laser (λ = 248 nm, pulse width 20 ns, and repetition rate = 10 Hz) operated at 350 mJ to ablate the target. The deposition temperature and pressure were 300 °C and $10^{-6}$ Torr, respectively. The substrate-target distance was 55 mm. All PLD parameters were kept constant for 30 min. The structural properties of the synthesized materials were determined using an X-ray diffraction spectrometer (Bruker AXS D8 Advance) equipped with Cu-Kα (λ = 1.5418 Å). To study the morphological properties, we used scanning electron microscopy (SEM) JSM-6700F: field emission scanning electron microscope with a spatial resolution of 1.1 nm and energy resolution of 137 eV. Raman spectra were obtained at room temperature using a confocal Raman microscope, Thermofisher DXR (3 lasers 532 nm, 633 nm, 785 nm).

## 3. Results

### 3.1. Structural Analysis

Figure 1 shows the results of XRD analysis of the nanoparticles and the thin layer of ZnO doped 3% cobalt. For the powder, the apparatus was the Bruker D8 Advanced X-ray diffractometer, and the X-ray radiation used was the copper K line with a wavelength of 1.5418 Å. The diffractogram of the sample contains diffraction peaks such as (100), (101), (102), (103), (200), (112), (201), (004), and (202), and correspond to the hexagonal wurtzite structure of ZnO with card No. 186, JCPDS no. 36-1451. No additional impurities were observed. Fig. 1(b) represents the diffractogram of 3% ZnO:Co thin film on Suprasil substrate. The thin layer of ZnO:Co deposited shows the presence of a preferential directional orientation (002), which corresponds to the crystallographic c axis perpendicular to the surface of the substrate. No peak associated with secondary phases is observed. The Rietveld refinement method analysis of XRD data of Co-doped ZnO powder and thin-film samples using the FullProf program are shown in Fig. 2. The refinement result showed that all samples crystallized in the space group P63mc hexagonal wurtzite structure. The fits between observed and calculated profiles are very good. The size of the crystallites, which influence the physical characteristics (electric, optical, etc.) of the samples, can be determined using diffraction analysis. Crystallite sizes were determined as a function of length at half-height using Scherrer's formula [23]:

$$\mathrm{D} = \frac{k\lambda}{\beta \cos\theta} \tag{1}$$

Here k = 0.9, which refers to spherical-shaped factor for ZnO species, λ = 1.5418 Å and θ is the angle at the maximum. The calculated strain is given by Eq. (2) [24]:

$$\varepsilon = \frac{c - c_0}{c_0} \times 100 \tag{2}$$

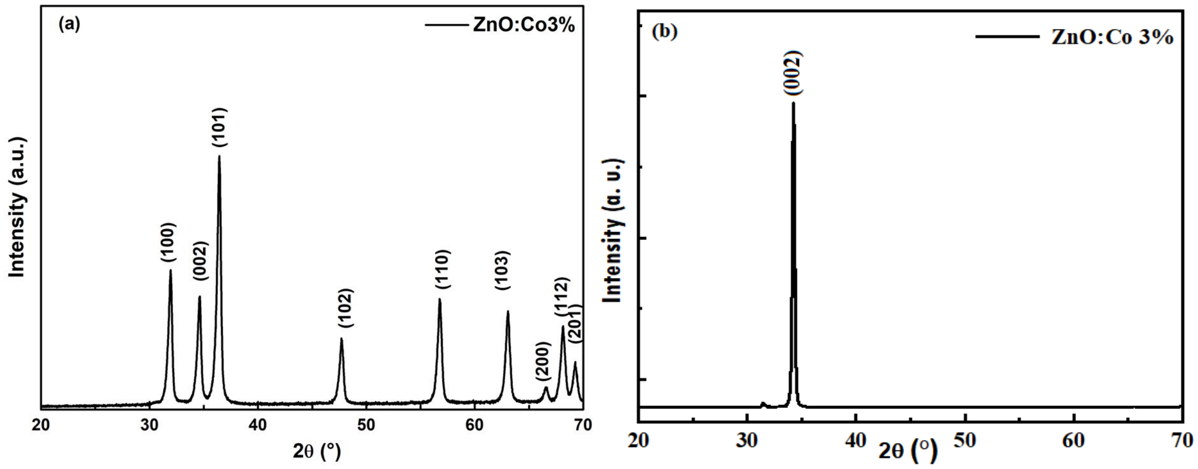

FIG. 1. XRD diffractograms of ZnO:Co with 3 at. % of cobalt a) Nanoparticles, b) Thin film.

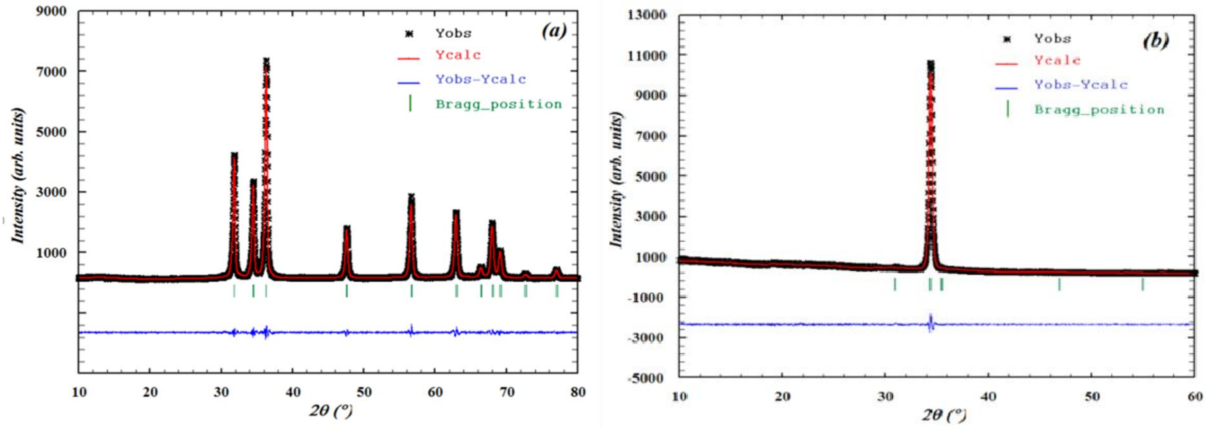

FIG. 2. XRD patterns at room temperature for Co-doped ZnO at. 3%: (a) Nanoparticles and (b) thin film by the Rietveld method.

The calculated deformation (ε) is given by Eq. (2). It is defined as a ratio of the difference in each lattice parameter between film and bulk crystal, where c is the lattice parameter of the sample, and $c_0$ = 0.52075 nm is the lattice parameter of undoped ZnO. The lattice parameter percentage change caused by doping is what this equation expresses, which shows the level of strain induced in the crystal structure.

The residual constraint is expressed as [25]:

$$\sigma = -233 \times \varepsilon \qquad (3)$$

Dislocation density is a parameter that directly shows the imperfection of the crystal lattice and it is related to the length of the dislocation line per unit of volume of the crystal. The dislocation density is written as follows [26]:

$$\delta = \frac{1}{D^2} \qquad (4)$$

where D is the crystallite's size. Table 1 depicts the lattice parameters (a, c) and volume of ZnO:Co nanoparticles and thin film obtained by the Rietveld method. A deviation in the parameters' values of (a) and (c) was observed compared to the literature [27]. It seems that the calculated parameters have tensile and compressive stresses when subjected to positive-to-negative stresses on the ZnO. Stress in ZnO:Co can be attributed to intrinsic factors such as impurities, defects, and distortions in the crystal lattice. X-ray diffraction (XRD) analysis showed a shift in the lattice parameters of the ZnO:Co thin film, indicating the presence of strain. This stress is likely intrinsic and correlates with the incorporation of Co dopants, which introduce local lattice distortions due to the difference in ionic radii between $Zn^{2+}$ (0.740 Å) and $Co^{2+}$ (0.745 Å) [28]. Fig. 3 shows the scanning electron microscope used to determine the morphological characteristics of the powder and the thin layer of ZnO:Co. The SEM image of the ZnO:Co nanopowder reveals spherical-shaped agglomerated particles, indicating the high surface energy of the nanoparticles, which promotes their clustering. The uniform grain size distribution suggests homogeneous nucleation during synthesis. Therefore, the SEM image of the ZnO:Co thin film shows a dense and smooth surface with a homogeneous grain distribution at the nanometric scale. The absence of cracks and porosities suggests good adhesion to the substrate. Additionally, the ZnO:Co nanopowder, with its high specific surface area due to nanoparticle agglomeration, is promising for applications in catalysis, gas sensing, and energy storage. Thus, the morphological analysis of both samples highlights characteristics that are appropriate for various advanced technological applications.

TABLE 1. Structural parameters of ZnO: Co 3 at.% nanoparticles and thin film.

| | ZnO:Co nanoparticles | ZnO:Co thin film |
|---|---|---|
| a = b (Å) | 3.245 | 3.25 |
| c (Å) | 5.197 | 5.225 |
| V (Å $^3$) | 47.404 | 47.75 |
| D (nm) | 22 | 33 |
| $\varepsilon$ (%) | -0.00184383 | 0.003533976 |
| $\sigma$ (GPa) | 0.429608 | -0.823416 |
| $\delta$(nm$^{-2}$) | 0.04545 | 0.03030 |

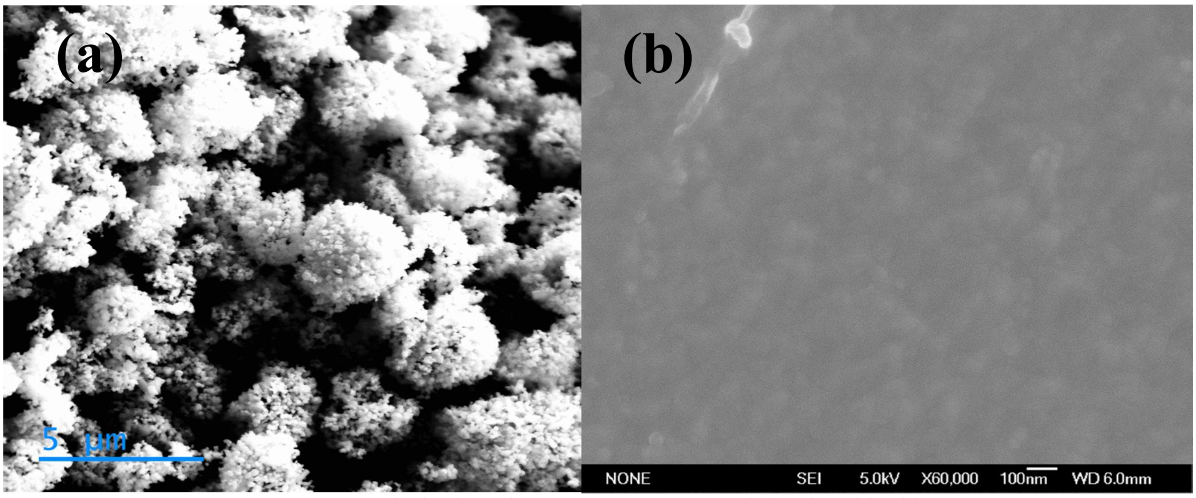

FIG. 3. Morphologies of ZnO:Co. a) Nanoparticles, b) Thin film.

### *3.2. XPS Analysis*

The structural properties, chemical composition and states of the thin film are studied by XPS photoelectron spectroscopy. Fig. 4(a) shows the XPS spectrum of 3% ZnO:Co thin film. Many peaks are detected in the XPS spectrum, confirming the existence of Zn, O, Co and a carbon-contaminated peak at 285 eV. Fig. 4(b) shows the high-resolution XPS spectrum Zn2p. This peak at 1022 eV is associated with Zn2p2/3, which consists of the Zn atom in the 2+ oxidation state [29]. The high-resolution XPS spectrum of O1s is presented in Fig. 4(c). After deconvolution, the peak is divided into two peaks: the $O_L$ peak at 530 eV is attributed to the oxidation of oxygen $O^{2-}$ in the Wurtzite structure of ZnO, and the $O_V$ peak at 532 eV corresponds to oxygen vacancies and zinc interstitials. Fig. 4(d) presents the high-resolution spectra of the Co 2p state, revealing two characteristic peaks at 781 eV and 797 eV, corresponding to Co 2p3/2 and Co 2p1/2, respectively. This indicates that Co 2p is in the $Co^{2+}$ oxidation state with tetrahedral coordination in the ZnO matrix. These results are confirmed by X-ray diffraction data, as well as by the presence of "shake-up" and "shake-off" satellite peaks at 787 eV and 803 eV, respectively, and the energy difference between Co2p3/2 and Co2p1/2, is equal to 15.5 eV. Based on high-resolution XPS measurements, the oxygen state was characterized. The results suggest that $Co^{2+}$ doping can enhance the formation of oxygen vacancies, which is beneficial for the exchange interaction in ZnO:Co, thereby improving the magnetism in ZnO.

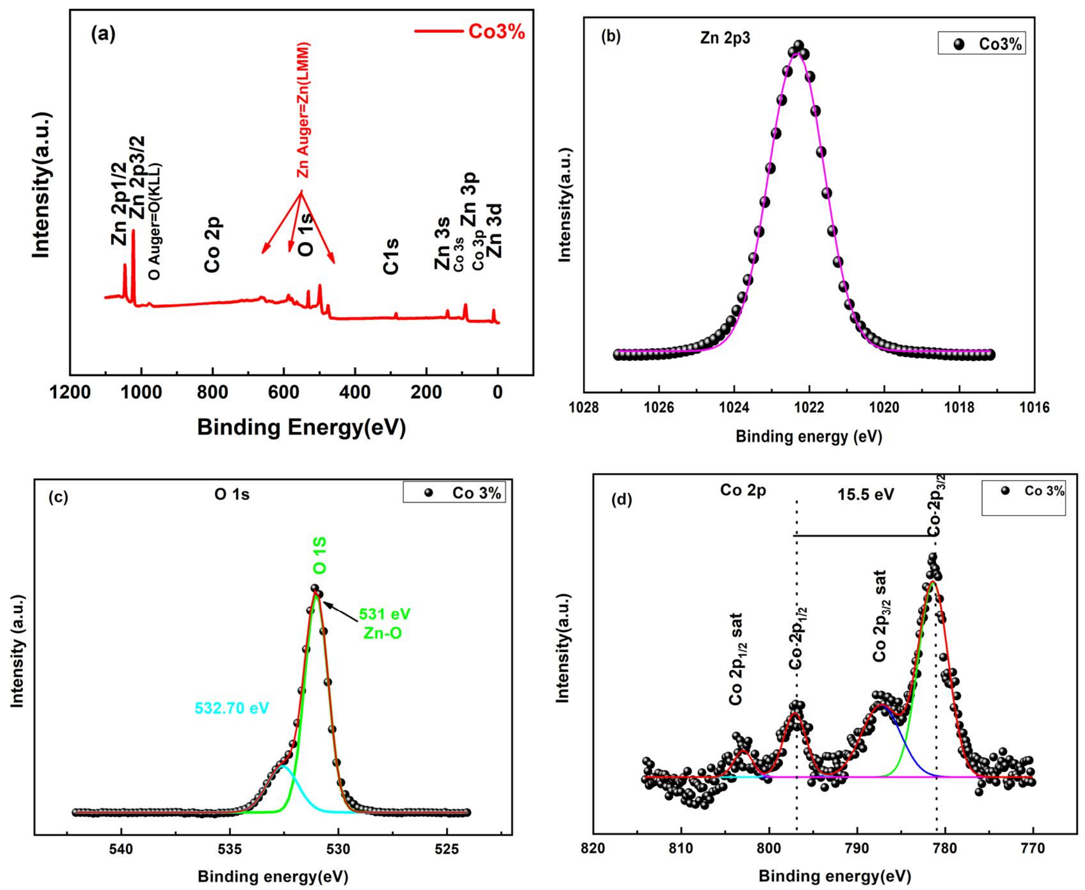

FIG. 4. (a) XPS survey scan spectra. High-resolution XPS of (b) Zn 2p, (c) O 1s, and (d) Co 2p state energies.

### *3.3. Optical Analysis*

Optical properties were investigated using UV–visible spectroscopy. Absorption curves for ZnO:Co nanoparticles and thin film as a function of wavelength are shown in Fig. 5. The ultraviolet region has high absorption due to band-to-band electronic transition. In the visible range, we have observed absorption bands that have three clear peak absorptions of ZnO-doped cobalt, and they are attributed to $^4A_2(F) \rightarrow {}^2A_1(G)$ (570 nm), $^4A_2(F) \rightarrow {}^4T_1(P)$ (613 nm) and $^4A_2(F) \rightarrow {}^2E(G)$ (660 nm) [18, 32, 33], and the observed infrared band is attributed to $^4A_2(F) \rightarrow {}^4T_1(F)$ transition. The $Zn^{2+}$ tetrahedral substitution sites in the ZnO host network coordinate the internal d-d transitions of the $Co^{2+}$ ions [34-36]. From the absorption spectra of two samples, we can calculate the absorption coefficient and gap energy by Tauc relation [37]:

$$(\alpha h\nu)^2 = A(h\nu - Eg) \quad (5)$$

where A is constant, $E_g$ is optical energy in eV, hν is the photon energy, and α is absorption coefficient ($cm^{-1}$). The evolution of $(\alpha h\nu)^2$ as a function of hν is shown in Fig. 6. The intersection of the line tangent with the abscissa axis gives the value of gap energy that is equal to 3.05 eV and 3.33 eV for ZnO:Co powder and thin film respectively, which is lower than the value of pure ZnO crystal as reported elsewhere [38]. The low value of the gap energy is explained in terms of the formation of the band tail [18, 19, 39]. This means the formation of a high density of donor levels near the conduction band, which confirms the presence of a high density of defects, particularly in the powder. Additionally, in general, tensile stress appears in the crystal as the band gap decreases, while the band gap value increases due to pressure stress; this is well confirmed in the literature. In our case, the results of the variations of the mesh parameters are presented in Table 2 [40]. The evolution of the band gap is due particularly to the band tail, which is reduced in the case of the thin film as a result of improvement of the crystallinity of the material and the reduction of the defect concentration, particularly on the surface. The decrease in defect densities depended on the compressive stress, the evolution of the crystallite size, and the value of the specific surface area [41].

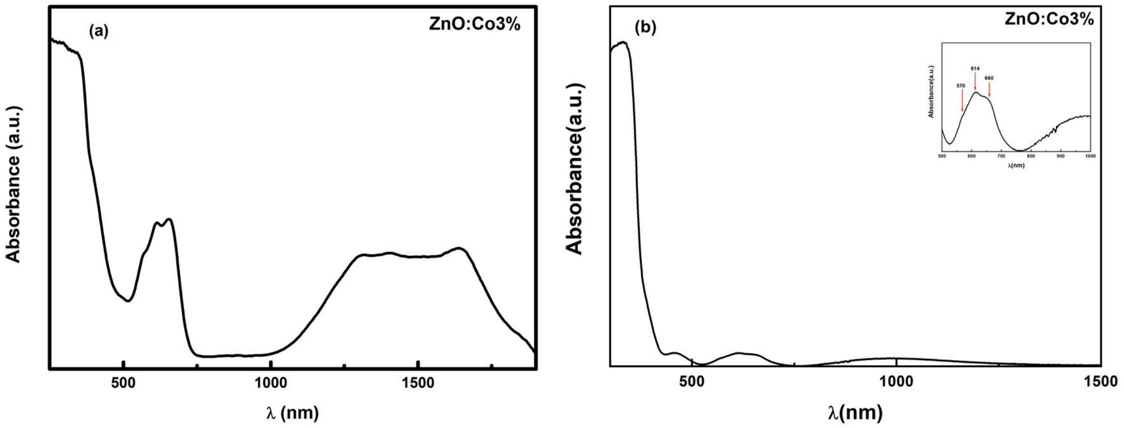

FIG. 5. Absorbance spectra of ZnO:Co. a) Nanoparticles, b) Thin film.

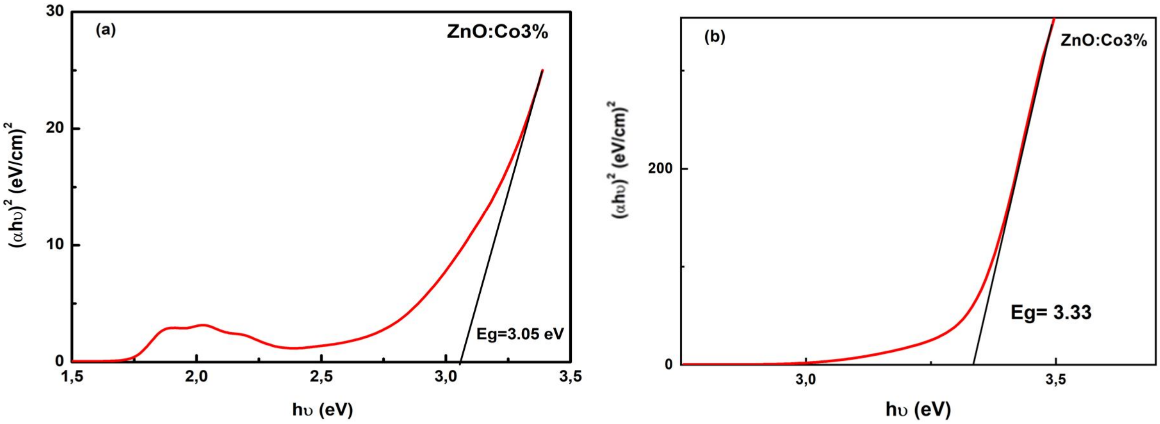

FIG. 6. Evolution of $(\alpha h\nu)^2$ as a function of hν of ZnO:Co. a) Nanoparticles, b) Thin film.

TABLE 2. Refinement parameters of ZnO: Co 3 at.% nanoparticles and thin film.

| | Samples | |
|---|---|---|
| Atomic coordinates | ZnO:Co nanoparticles | ZnO:Co thin film |
| Zn | | |
| x | 0.3333 | 0.3333 |
| y | 0.6667 | 0.6667 |
| z | 0.5000 | 0.5000 |
| Occ. | 0.970 | 0.970 |
| Co | | |
| x | 0.3333 | 0.3333 |
| y | 0.6667 | 0.6667 |
| z | 0.5000 | 0.5000 |
| Occ. | 0.030 | 0.030 |
| O | | |
| x | 0.3333 | 0.3333 |
| y | 0.6667 | 0.6667 |
| z | 0.88243 (8) | 0.8808 (8) |
| Occ. | 0.947 | 1.000 |
| Agreement factors | | |
| $R_p$ (%) | 6.49 | 3.10 |
| $R_{wp}$ (%) | 8.20 | 4.17 |
| $R_{exp}$ (%) | 5.89 | 4.11 |
| $\chi^2$ | 1.93 | 1.03 |

### *3.4. Raman Study*

In the wurtzite structure, zinc oxide consists of four atoms (two molecular units of Zn-O). At the point, Γ of the Brillouin zone, the optical phonons have the irreducible representation $\Gamma_{opt} = A_1 + 2B_1 + E_1 + 2E_1$, which explains why the polar modes $A_1$ and $E_1$ are both active in the Raman and infrared and divide into longitudinal and transversal optical components. Their vibrations are polarizable and doubly degenerate, and the $B_1$ are silent modes. These phonons are caused by the number of atoms (3n = 12) and three acoustic modes (1* LA, 2*TA) and n-3=9 optical phonons (3LO, 6TO). Fig. 7 depicts the Raman spectra of ZnO:Co nanoparticles and thin films using an excitation wavelength of λ = 532 nm. Several peaks were identified in the ZnO Raman spectrum: peaks at 367 $cm^{-1}$, 430 $cm^{-1}$, and 564 $cm^{-1}$, corresponding to $A_1$ (TO), $E_2$ (high), and $E_1$ (LO) modes, respectively. The $A_1$ (TO) mode corresponds to a vibration mode, while the $E_2$ (high) peak indicates the wurtzite crystal structure of ZnO, showing good crystallinity in both samples [42]. A relationship exists between stress and the $E_2$ (high) mode; under compressive stress, the $E_2$ (high) peak shifts to a higher value. The shift of the $E_2$ (high) mode can provide valuable information about stress, as noted in the literature. When ZnO transitions from nanoparticles to a thin film, as revealed by XRD analysis, it exhibits tensile stress. This is evidenced by a greater shift in the $E_2$ (high) mode in the Raman spectrum, indicating lattice distortion of ZnO under tension. The $E_1$ (LO) mode is associated with the formation of zinc interstitials and oxygen vacancies. The lower intensity of this peak in the thin film suggests a reduced defect density. This may be explained by the difference in material quantity. As the intensity of the $E_1$ (LO) mode narrows, the energy band gap increases from the thin film to the nanoparticles, indicating a reduction in oxygen vacancies and zinc interstitials. These results suggest that the presence of defects in ZnO could be utilized for various technological applications, such as gas sensors and photocatalysis [43, 44].

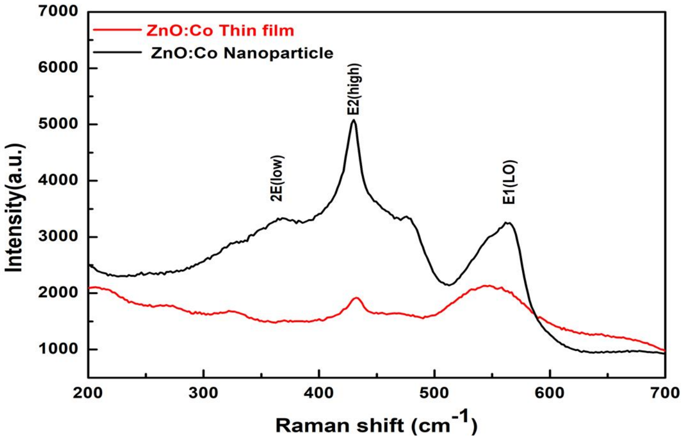

FIG. 7. Raman spectra of ZnO:Co nanoparticles and thin film under λ = 532 nm of laser beam wavelength.

## 4. Conclusion

ZnO:Co with a cobalt content of 3 atomic percent nanoparticles was synthesized using the sol-gel method. In the second step, the obtained nanopowder was deposited as a thin film using PLD. Different techniques were used to characterize the two samples. The Co-doped ZnO nanoparticles exhibit minor compressive stress, which is changed to tensile stress in the case of a thin film, according to the XRD study conducted at 2θ. The presence of Zn, Co, and O was detected by X-ray photoelectron spectroscopy (XPS). The pattern of change of the energy band gap indicates a shift in the band structure of the ZnO:Co and provides information on the stress and defect concentration. An enhancement in the energy band gap is due to the improvement of the crystallinity of the material and the reduction of the defect concentration. The changes in the E2 (high) optical phonon mode of ZnO nanoparticles show how stress influences the wurtzite structure. Additionally, the peak at 536 $cm^{-1}$ observed in the Raman spectra confirms the presence of oxygen vacancies in ZnO:Co. These results imply that laser ablation can be used to manage the different properties of ZnO:Co thin film-based aerogel, producing high-quality samples with improved and tunable structural properties.

## References

[1] Alzamzouma, T., Nahilia, M., Falaha, A., and Al-Raeei, M., Jordan J. Phys., 17 (2024) 577.

[2] Pearton, S.J., Abernathy, C.R., Overberg, M.E., Thaler, G.T., Norton, D.P., Theodoropoulou, N., and Hebard, A.F., Journal of Applied Physics, 93 (2003) 1.

[3] Ayadi, Z.B., Mahdhi, H., Djessas, K., Gauffier, J.L., El Mir, L., and Alaya, S., Thin Solid Films, 553 (2014) 123.

[4] Omri, K., Najeh, I., and El Mir, L., Ceramics International, 42 (2016) 8940.

[5] Hjiri, M., Aida, M.S., Lemine, O.M., and El Mir, L., Materials Science in Semiconductor Processing, 89 (2019) 149.

[6] El Ghoul. J., Barthou. C., Saadoun. M., and El Mir, L., Physica B: Condensed Matter, 405 (2010) 597.

[7] Jaballah, S., Benamara, M., Dahman, H., Ly, A., Lahem, D., Debliquy, M., and El Mir, L., Materials Chemistry and Physics, 255 (2020) 123643.

[8] El Mir, L., Journal of Luminescence, 186 (2017) 98.

[9] Rasouli, S. and Moeen, S.J., Journal of Alloys and Compounds, 509 (2011) 1915.

[10] Cui, J.B., Soo, Y.C., and Chen, T.P., Journal of Physical Chemistry C, 112 (2008) 4475.

[11] Alyamani, A., Tataroğlu, A., El Mir, L., Al-Ghamdi, A.A., Dahman, H., and Farooq, W.A., Applied Physics A, 122 (2016) 1.

[12] El Mir, L., Journal of Inorganic and Organometallic Polymers and Materials, 31 (6) (2021) 2648.

[13] Chen, Q. and Wang, J.L., Chemical Physics Letters, 474 (2009) 336.

[14] Peng, W.Q., Qu, S.C., Cong, G.W., and Wang, Z.G., Materials Science in Semiconductor Processing, 9 (2006) 156.

[15] Krithiga, R. and Chandrasekaran, G., Crystal Growth and Design, 311 (2009) 4610.

[16] Maensiri, S., Masingboon, Ch., Promarak, V., and Seraphin, S., Optical Materials, 29 (2007) 1700.

[17] Krithiga, R. and Chandrasekaran, G., Journal of Crystal Growth, 311 (2009) 4610.

[18] Khlifi, N., Ihzaz, N., Mrabet, S., Alyamani, A., and El Mir, L., Journal of Luminescence, 245 (2022) 118770.

[19] Mrabet, S., Ihzaz, N., Alshammaric, M., Khlifi, N., Ba, M., Bessadok, M.N., Mejri, I.H., and El Mir, L., Journal of Alloys and Compounds, 920 (2022) 165920.

[20] El Mir, L. and Omri, K., Superlattices and Microstructures, 75 (2014) 89

[21] El Mir, L., Amlouk, A., Barthou, C., and Alaya, S., Physica B, 388 (2007) 412.

[22] Omri, K., Alyamani, A., and El Mir, L., Journal of Materials Science: Materials in Electronics, 30 (2019) 16606.

[23] Slama, R., El Ghoul, J., Omri, K., Houas, A., El Mir, L., and Launay, F., Journal of Materials Science: Materials in Electronics, 27 (2016) 7939.

[24] Caglar, Y., Journal of Alloys and Compounds, 560 (2013) 181.

[25] Sathya, M. and Pushpanathan, K., Journal of Alloys and Compounds, 449 (2018) 346.

[26] Benramachea, S., Benhaoua, B., and Belahssena, O., Optik, 125 (2014) 5864.

[27] Robkhob, P., Tang, M., and Thongmee, S., Journal of Superconductivity and Novel Magnetism, 32 (2019) 3637.

[28] Malek, M.F., Mamat, M.H., Khusaimi, M., Sahdan, M.Z., Musa, M.Z., Zainun, A.R., Suriani, A.B., Md Sin, N.D., Abd Hamid, S.B., and Rusop, M., Journal of Alloys and Compounds, 582 (2014) 12.

[29] Caglar, Y., J., Journal of Alloys and Compounds, 560 (2013) 181.

[30] Pazhanivelu, V., Selvadurai, A.P.B., Murugaraj, R., Muthuselvam, P., and Chou, F.C., Journal of Materials Science: Materials in Electronics, 27 (2016) 8580.

[31] Ye, J.D., Gu, S.L., Qin, F., Zhu, S.M., Liu, S.M., Zhou, X., Liu, W., Hu, L.Q., Zhang, R., Shi, Y., Zheng, Y.D., and Ye, Y.D., Applied Physics A - Materials, 81 (2005) 809.

[32] Ghribi, F., Khalifi, N., Mrabet, S., Ghiloufi, I.¸ Talu, S., El Mir, L.M., da FonsecaFilho, H.D., Oliveira, R.M.P.B., and Matos, R.S., Arabian Journal for Science and Engineering, 47 (2022) 7717.

[33] El Mir, L., Ben Ayadi, Z., Rahmouni, H., El Ghoul, J., Djessas K., and von Bardeleben, H.J., Thin Solid Films, 517 (2009) 6007.

[34] Valerio, L.R., Mamani, N.C., de Zevallos, A.O., Mesquita, A., Bernardi, M.I.B., Doriguetto, A.C., and de Carvalho, H.B., RSC Advances, 7 (2007) 20611.

[35] Roguai, S., Djelloul, A., Souier, T., Dakhel, A.A., and Bououdina, M., Journal of Alloys and Compounds, 599 (2014) 150.

[36] Kang, S., Kim, Y., Eunkyung Kim, S., and Kim, S., Journal of Electronic Materials, 9 (2013) 3.

[37] Wang, W., Zhang, F., Wang, X., Zhang, S., Yan, J., and Zhang, W., European Journal of Physics, 135 (2020) 1.

[38] Omri, K., Najeh, I., Dhahri, R., El Ghoul, J., and El Mir, L., Microelectronic Engineering, 128 (2014) 53.

[39] Kumar, S., Basu, S., Rana, B., Barman, A., Chatterjee, S., Jha, S.N., Bhattacharyya, D., Sahoo, N.K., and Ghosh, A.K., Journal of Materials Chemistry C, 3 (2014) 481.

[40] Scepanovic, M., Grujic-Brojcin, M., Vojisavljevic, K., Bernik, S., and Sreckovic, T., Raman Spectroscopy, 41 (2010) 914.

[41] Kim, K.K., Koguchi, N., Ok, Y.W., Seong, T.Y., and Park, S.J., Applied Physics Letters, 84 (2004) 3810.

[42] Achehboune, M., Khenfouch, M., Boukhoubza, I., Leontie, L., Doroftei, C., Carlescu, A., Bulai, G., Mothudi, B., Zorkani, I., and Jorio, A., Materials Today, 53 (2022) 319.

[43] Ren, H., Xiang, G., Gu, G., and Zhang, X., Materials Letters, 122 (2014) 256.

[44] Bu, I.Y.Y., Superlattices and Microstructures, 75 (2014) 657.